

Dual-Polarity slice-GRAPPA for concurrent ghost correction and slice separation in Simultaneous Multi-Slice EPI

W. Scott Hoge¹, Kawin Setsompop^{2,3}, Jonathan R. Polimeni^{2,3}

(1) Department of Radiology, Brigham and Women's Hospital and Harvard Medical School, Boston, MA, USA.

(2) Athinoula A. Martinos Center for Biomedical Imaging, Department of Radiology, Harvard Medical School, Massachusetts General Hospital, Charlestown, MA, USA.

(3) Harvard-MIT Division of Health Sciences and Technology, Massachusetts Institute of Technology, Cambridge, MA, USA.

Address correspondence to: shoge@bwh.harvard.edu

Purpose: A ghost correction strategy for Simultaneous Multi-Slice (SMS) EPI methods that provides improved ghosting artifact reduction compared to conventional methods is presented. Conventional Nyquist ghost correction methods for SMS-EPI rely on navigator data that contain phase errors from all slices in the simultaneously-acquired slice-group. These navigator data may contain spatially non-linear phase differences near regions of B_0 inhomogeneity, which violates the linear model employed by most EPI ghost correction algorithms, resulting in poor reconstructions.

Methods: Dual-Polarity GRAPPA (DPG) was previously shown to accurately model and correct both spatially non-linear and 2D phase errors in conventional single-slice EPI data. Here, an extension we call Dual-Polarity slice-GRAPPA (DPsG) is adapted to the slice-GRAPPA method and applied to SMS-EPI data for slice separation and ghost correction concurrently—eliminating the need for a separate ghost correction step while also providing improved slice-specific EPI phase error correction.

Results: Images from *in vivo* SMS-EPI data reconstructed using DPsG in place of conventional Nyquist ghost correction and slice-GRAPPA are presented. DPsG is shown to reduce ghosting artifacts and provide improved temporal SNR compared to the conventional reconstruction.

Conclusion: The proposed use of DPsG for SMS-EPI reconstruction can provide images with lower artifact levels, higher image fidelity, and improved time-series stability compared to conventional reconstruction methods.

Key words: Nyquist Ghost Correction, Parallel Imaging, Blipped-CAIPI, MultiBand EPI

INTRODUCTION

Echo Planar Imaging (EPI) is widely used across a full spectrum of neuroimaging applications, including functional, diffusion, and perfusion imaging. For example, in functional MRI (fMRI), EPI is well-suited to image the temporal dynamics of the hemodynamic response to brain function, and can be readily sensitized to local changes in blood flow and oxygenation. The temporal resolution of the EPI acquisition is limited, however, by the time required to achieve full-brain coverage with a stack of 2D image slices. Simultaneous Multi-Slice (SMS) EPI [1–5] has recently gained wide acceptance due to its ability to accelerate the acquisition of multiple slices in an otherwise conventional EPI pulse sequence, and thereby either increase the temporal acquisition rate of EPI data for a fixed spatial coverage in the slice direction or extend spatial coverage for a fixed temporal acquisition

rate. In SMS imaging, multiple image slices are excited simultaneously using MultiBand slice-selective RF pulses, and the resulting signal reflecting the collapsed slices is measured [2, 6–8]. Parallel image reconstruction methods such as those based on 2D SENSE [9] or slice-GRAPPA [8] are then used to separate individual slices from the collapsed group of simultaneously-acquired slices. SMS-EPI provides the advantage of improved imaging efficiency with limited SNR penalty. This is in contrast with other accelerated imaging methods, such as conventional parallel imaging [10], which instead undersample k-space to reduce the amount of data needed to form an image. To improve image quality and reduce g-factor penalty, CAIPIRINHA techniques [11], notably the blipped-CAIPI method [8], can be integrated into EPI.

All EPI-based methods suffer from inherent imaging artifacts. In the case of SMS-EPI, correcting inherent EPI Nyquist ghosts can be particularly challenging [8, 12]. Nyquist ghosts arise from sampling differences between data that are sampled on positive, RO^+ , versus negative, RO^- , polarity readout gradients. The dominant effect is a shift between the respective sampling grids in k-space, or equivalently, via the Fourier shift theorem, a linear ramp along x in the $x-k_y$ hybrid-space representation of the phase difference between data sampled using RO^+ and RO^- readout gradients. However, non-linear phase differences between these measured data can also occur, such that the phase difference between RO^+ and RO^- data does not vary linearly along the x direction, particularly when sampling near regions of local field inhomogeneity [13]. These non-linear phase errors result in image artifacts when standard Nyquist ghost correction (NGC) methods that assume a linear phase error are applied. When present, these artifacts are compounded in SMS-EPI because non-linear phase errors that exist in one slice may bias the phase error estimation for the entire slice-group when traditional phase navigator signals for NGC are employed, degrading the ghost correction performance for all slices. It has been long recognized that phase errors can vary across different EPI slices, and therefore slice-specific ghost correction is recommended [14]. This can be challenging in SMS-EPI because the phase correction navigators are often acquired with the SMS-EPI data and therefore this navigator data is collapsed across the simultaneously-acquired slices, which causes the slice-specific information to be lost [2, 3]. It has been shown that SMS-EPI image quality can be improved when slice-specific ghost correc-

tion is integrated into the slice separation stage of both SENSE-based [15, 16], GRAPPA-based [8], and hybrid [17] reconstruction methods. Although slice-specific ghost correction may not always be needed, we have found this approach can lead to improvement in both conventional clinical/research scanners (as shown in Ref. [3]) and special-purpose scanners (e.g. the scanner described in Ref. [18]).

Dual-Polarity GRAPPA (DPG) [13] is a recently-proposed EPI ghost correction method designed to address non-linear phase errors. DPG employs GRAPPA-based [19] convolution kernels that draw directly from data measured on RO^+ and RO^- readout gradients to accurately model and correct both spatially non-linear and 2D phase errors. Here we introduce a DPG-based approach to reconstruct SMS-EPI data. We demonstrate that this extension of DPG to slice-GRAPPA can be used to separate collapsed slices while concurrently performing slice-specific ghost correction. This yields reconstructed images with lower levels of RO^+ -vs- RO^- phase-error artifacts than can be achieved with current conventional approaches that typically rely on linear models [3].

THEORY

A review of image reconstruction from SMS-EPI data using slice-GRAPPA

SMS-EPI is typically acquired with controlled aliasing using blipped-CAIPI to improve parallel imaging performance. The use of slice-GRAPPA to reconstruct images from blipped-CAIPI SMS-EPI data requires multiple phase correction steps to ensure that individual slices can be correctly extracted and reconstructed from the measured group of simultaneously-acquired slices (hereafter called a *slice-group*). Our application of DPG to SMS-EPI employs similar steps, which are briefly reviewed below.

First, a blipped-CAIPI SMS acquisition employs MultiBand RF excitation pulses along with gradient blips along the z direction during image encoding. The z -gradient blips impose a CAIPI shift along the phase-encoded direction, which shifts the relative FOV of each individual slice in the collapsed slice-group to yield a more favorable aliasing pattern in the collapsed data. In order to have the measured calibration data match this slice shifting, a *relative* phase shift is applied to the calibration data to induce an FOV shift that will match the slice shift present in each slice of the measured collapsed slice-group SMS data. Second, an *absolute* phase factor is imposed when the SMS data are sampled. This absolute phase is imparted by the z -gradient blipping and is a function of the absolute position of each slice relative to the scanner iso-center—the point where the gradient fields pass through zero—and needs to be removed from the acquired SMS-EPI data prior to slice separation. Finally, once the slice separation and in-plane data recovery has been performed, the relative phase shift in the reconstructed slices is removed. This step effectively removes the FOV shift imposed on each slice during acquisition to recenter each reconstructed image to its proper location within the object.

As mentioned above, ghost correction of SMS-EPI data is complicated by the fact that the RO^+ -vs- RO^- phase errors may be different for each slice in the measured collapsed slice-group.

Further, the phase correction navigator lines typically acquired at the beginning of each SMS-EPI readout are also collapsed across slices within a slice-group. A 2-kernel approach to this problem was recently proposed [3], and is employed in the slice-GRAPPA comparison images shown below. The primary difference between the 2-kernel slice-GRAPPA and DPoSG approaches to separating collapsed slices is that the 2-kernel method *preserves* the phase difference between RO^+ and RO^- lines to allow for subsequent slice-specific NGC using standard methods, whereas the DPoSG method *corrects* the phase difference by embedding slice-specific NGC into the slice-GRAPPA kernels. To preserve phase differences during slice separation, the previously proposed 2-kernel slice-GRAPPA approach recognizes that in single-shot EPI, phase errors alternate line by line across the k_y direction. This means that target locations along RO^+ lines are surrounded by a different pattern of phase errors along the k_y direction than target locations along the RO^- lines—for instance, target locations corresponding to data acquired along RO^+ readouts are flanked in the phase-encoding direction by RO^- readouts, while target locations corresponding to RO^- readouts are flanked by RO^+ readouts. The 2-kernel approach therefore seeks to train and apply separate kernels for each of the two possible patterns of phase errors in the immediate neighborhood of target points, so that the slice separation preserves the alternating phase errors across the k_y direction. It achieves this by training two kernels: one kernel centered on RO^+ lines and the other kernel centered on RO^- lines using a single frame of reference data (see Fig. 2F of Ref. [3]). Then, after the slice separation, conventional NGC can be applied to each slice. This approach accommodates any residual phase errors between RO^+ and RO^- data within the single-band reference data set. This is preferable to the single-kernel slice-GRAPPA approach, which causes a mixture of RO^+ and RO^- phase errors in the separated slices, complicating subsequent ghost correction. After slice separation, conventional phase correction is applied to each reconstructed slice separately, based on linear and constant phase correction coefficients derived from both the calibration data acquired at the beginning of each run and dynamic updates provided by navigator data acquired prior to each slice-group acquisition. This entire process is referred to below as “tailored ghost correction” [3].

In conventional slice-GRAPPA, single-band reference data are acquired for calibration. Synthesized SMS data are then formed via a summed version of the reference data using slices corresponding to each measured slice-group (with appropriate phase terms added to match the CAIPI shifting, as described above). A linear transform between each synthesized collapsed slice-group and the individual slices is then computed. Recent implementations of SMS-EPI use the LeakBlock [20] framework for this computation, which employs a “split” linear system for the GRAPPA coefficients to minimize errors from both image artifacts and inter-slice signal leakage [21]. LeakBlock has been shown to greatly reduce the amount of SMS cross-talk in fMRI experiments [22], and is compatible with the DPoSG approach presented below.

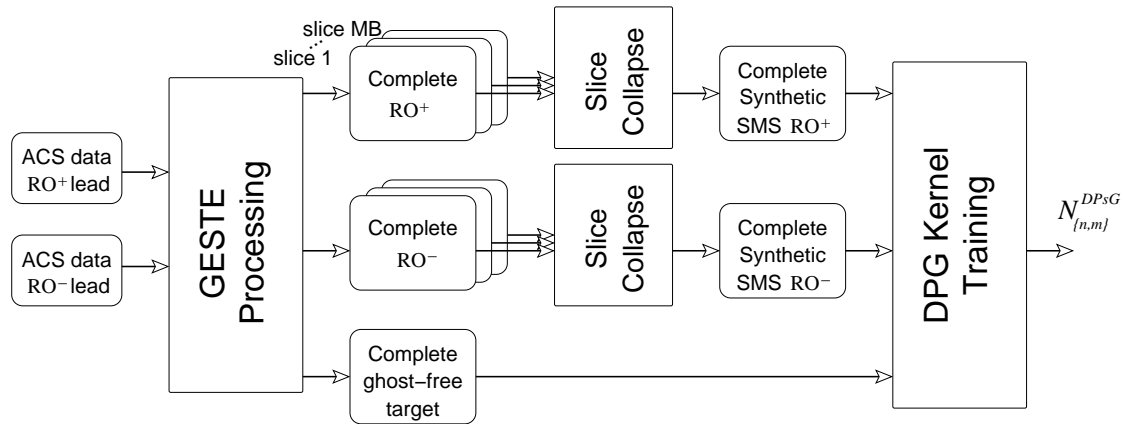


Figure 1. An illustration of the DP&S;G kernel calibration signal flow. From the left, temporally-encoded calibration data is sorted by readout polarity to form RO⁺ and RO⁻ images and a ghost-free GESTE target image for each slice. Multiple slices are then combined to form synthetic slice-group image data. From these three image data, DP&S;G kernels, $N_{\{n,m\}}$ for slice m of slice-group n , are formed by solving a LeakBlock-style linear system.

Formulation of DPG for SMS reconstruction

The extension of DPG to SMS-EPI data follows a simple change to the original DPG calibration process [13]. For the calibration of the DPG reconstruction kernels in this work, we employed (i) segmented EPI calibration data to match the echo spacing and echo time of the acquired SMS data. This ensures that the geometric distortion and phase characteristics present in the calibration data are well matched to the accelerated data. We also employed (ii) temporal encoding (i.e. two acquisitions of each EPI frame with reversed readout polarity), to remove *static* system errors via the GESTE method [23], and (iii) FLEET acquisition ordering [24] to limit the effects of *dynamic* errors that occur between EPI segments in the calibration data, such as those caused by subject motion or respiration. The temporal order for these sequence loop, from most-rapid to least-rapid, was (segment < polarity < slice) to improve robustness to motion in calibration data. For each slice, the RO⁺ and RO⁻ data from each segment are separated and interleaved to form fully-sampled images—complete frames of k-space that satisfy the Nyquist sampling criteria along k_y —for calibration source data. To generate calibration target data, the complete RO⁺ and RO⁻ images are phase corrected and coherently combined using GESTE to form ghost-free target images for each slice, sketched in Fig. 1 with a detailed illustration available in supplementary Figure S1.

Once the RO⁺/RO⁻ source and ghost-free target data have been formed from the temporally-encoded EPI segments, synthetic collapsed slice-groups were generated separately for both RO⁺ and RO⁻ source data. As in the slice-GRAPPA method, individual slices were FOV-shifted as needed prior to forming the synthetic collapsed slice-groups. Once the appropriate source and target images were synthesized, the DPG reconstruction parameters were generated by forming a LeakBlock [20] linear system of equations that map synthetic collapsed RO⁺ and RO⁻ source data to ghost-free target data for each slice. As with slice-GRAPPA, the calibration process is repeated for each individual slice-group to generate slice-specific DP&S;G kernels.

Schematics of four $2k_y$ -by- $5k_x$, DP&S;G kernels for the $R = 2$

case are shown in Fig. 2a. They illustrate a mapping of source points from both RO⁺ and RO⁻ sampled collapsed-slice k-space data to a target point in the single-slice reconstruction. The kernels in this example estimate data at k-space locations with both sampled (Kernels #1 and #3) and un-sampled (Kernels #2 and #4) phase-encoding lines. In EPI, data misalignment between the RO⁺ and RO⁻ sampled data will generate Nyquist ghosts. In conventional EPI, appropriate DPG kernels applied to the raw EPI data will properly align the sampled data to a common k-space grid, and in the process remove the measurement errors that produce Nyquist ghosts. In SMS EPI, this ghost correction feature is embedded within the DP&S;G kernel and combined with the slice-separation operation.

Once formed, the DP&S;G reconstruction parameters were then applied to measured SMS-EPI data. The reconstruction of each acquired collapsed slice-group was performed by first removing the absolute phase imposed on the slice-group data due to CAIPI FOV shifting, as described above. Appropriate DP&S;G kernels were then convolved with the data to yield a fully-sampled and ghost-corrected ensemble of images for each slice in the slice-group and for each channel in the receive coil array, as illustrated in Fig. 2b. The relative phase in FOV-shifted slices was then removed to return the images to the correct location within the FOV. Finally, the individual images for each coil channel were combined via the standard root-sum-of-squares combination.

Because DPG is derived from GRAPPA, one can use DPG kernels to perform in-plane data recovery in addition to the slice separation and ghost correction functions in a single one-stage reconstruction pass, as shown in Fig. 2b. Alternatively, one can employ DP&S;G for only the later functions, and employ standard GRAPPA for in-plane accelerated data recovery in a two-stage reconstruction. Note that with the two-stage reconstruction the in-plane-GRAPPA step will operate on ghost-free data, as the DP&S;G reconstruction in the first stage removes ghosting. In this case, in-plane-GRAPPA kernels should be trained on ghost-free calibration data for both source and target [25]. We tested both the one-stage and two-stage approaches but found no significant image quality advantage to either approach (see Discussion).

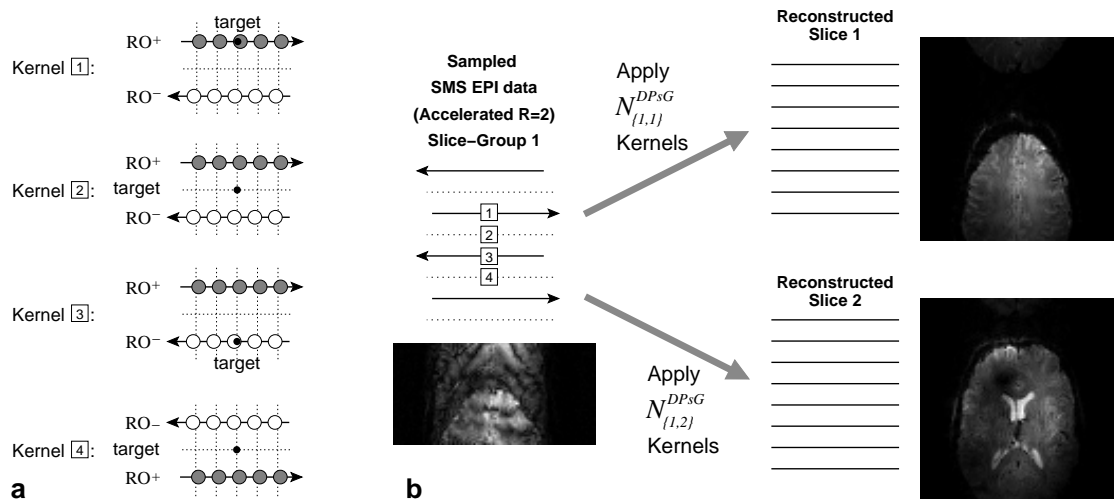


Figure 2. An illustration of the DPG reconstruction process for $R = 2$ source data. A set of $2k_y$ -by- $5k_x$ sized DPG kernels needed for the reconstruction of a single slice are shown in (a). Gray filled circles represent multi-channel RO⁺ source SMS data, white filled circles represent multi-channel RO⁻ source SMS data, and the small black filled points represent target locations in the single-slice, single-coil estimate. (To aid in readability, the coil and slice dimensions of the full data extent are not shown.) The source points are shown offset from the sampling grid to represent phase errors along the readout direction, which alternate in polarity between RO⁺ and RO⁻ lines. The locations where each of these kernels are applied are shown in (b), where the numbered squares correspond to the kernels illustrated in (a). Note that kernels 1 and 3 estimate data on k-space grid locations corresponding to sampled data, while kernels 2 and 4 each estimate data for un-sampled k-space grid locations. Note that kernel 2 employs a RO⁺/RO⁻ source data pattern that is different from kernel 4 for recovery of in-plane acceleration. The recovery of each slice within a measured SMS slice group is achieved via convolution kernels specific to each output slice.

Therefore, all images presented below corresponding to datasets with both in-plane and slice acceleration were reconstructed with the two-stage approach.

METHODS

Data acquisition

All human *in vivo* data were acquired in healthy volunteers upon written informed consent.

EPI data at different MultiBand (MB) factors and in-plane acceleration rates, R , were acquired using an in-house SMS sequence implementation on a 7 Tesla (7T) whole-body scanner (Siemens Healthcare, Erlangen, Germany) equipped with a custom-built 32-channel brain array receive coil, and a birdcage transmit coil [26]. Data with no in-plane acceleration was acquired with matrix size: 64×128 , FOV: 19.2 cm^2 , in-plane resolution: $3 \text{ mm} \times 1.5 \text{ mm}$, slice thickness: 1.5 mm , $R = 1$, MB-3, TR=0.825 s, TE=29 ms, 39 slices, 75 volumes. A 2.2 mm isotropic resolution data set was acquired at $R = 2$, MB-3, FOV/3 CAIPI-shift, TR=1 s, TE=25 ms, matrix size: 96×96 , FOV: 21.2 cm^2 , 39 slices, 75 volumes. Higher-resolution data were acquired from two subjects with 1.5 mm isotropic spatial resolution, matrix size: 128×128 , FOV: 19.2 cm^2 , $R = 3$, MB-2, FOV/2 CAIPI-shift, TR=1.2 s, TE=22 ms, 46 slices, 75 volumes.

Additional data were acquired *in vivo* using a 3 Tesla (3T) “Connectom” whole-body scanner (Siemens Healthcare, Erlangen, Germany) equipped with 300 mT/m gradients [27] and a custom-built 64-channel brain array receive coil [28]. This data set employed a sagittally-zoomed diffusion-weighted SMS-EPI

sequence [29, 30] with phase encoding along the S-I direction, TR=5 s, $R = 2$, MB-3, FOV/3 CAIPI-shift, 1.5 mm isotropic resolution, $22.2 \text{ cm} \times 13.2 \text{ cm}$ FOV, matrix size: 148×88 , 225 diffusion directions, and 75 sagittal slices.

Image reconstruction

In each example presented below, a DPG kernel of size $3k_y$ -by- $5k_x$ was employed for slice separation. For in-plane data recovery, a $2k_y$ -by- $5k_x$ GRAPPA kernel, trained on the ghost-free calibration data (provided by GESTE) as source and target data, was performed subsequent to slice separation in a two-stage GRAPPA-based reconstruction. DPG images were reconstructed with a MATLAB (MathWorks, Natick, MA, USA) implementation running on an 64-bit Linux machine with 16 GB of RAM and an 8-core CPU. For comparison, images reconstructed with current state-of-the-art methods were generated by both the in-house developed (7T) and vendor-supplied (3T Connectom) online slice-GRAPPA-based SMS-EPI reconstruction (Siemens WIP 770A), both of which employed a tailored ghost correction approach and Local Phase Correction (LPC) [31] for estimation of the linear phase error between RO⁺ and RO⁻ data. A software implementation of the image reconstruction described here is available upon request.

Image post-processing

The 3T Connectom data presented in the Results below exhibit clear 2D phase errors attributable to eddy currents and/or asymmetric gradient timing errors across the three gradient coil axes that cause ghosting in oblique slice prescriptions. Errors

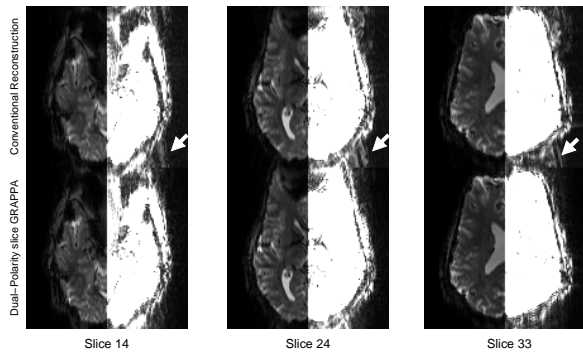


Figure 3. A comparison between current conventional SMS-EPI image reconstruction and DPoS image reconstruction from the $R = 1$, MB-3 *in vivo* data. The right-half of each slice shows the lowest 10% of signal to emphasize ghosting. Ghosting levels in the DPoS images are notably lower in regions indicated by arrows. Mosaic images that compare the complete volume are provided in Figure S2, available on-line in the Supplemental media files.

of this type cannot be corrected using common NGC methods based on 1D linear models. To better visualize and analyze these errors, we employed the Virtual Body Coil (VBC) method of Buehrer, et al. [32], to combine the multiple coil images into a single image while preserving relative image phase. The VBC coil combination parameters were identified for one central slice, and then deployed for all other slices, to maintain consistent coil combinations for all slices. To quantify the relative Δk shift along k_x and k_y corresponding to the 2D phase error, we computed a singular value decomposition (SVD) of the 2D phase error plane to generate a rank-1 estimate and then used LPC to estimate the phase slope in each singular vector separately, which corresponds directly to the amount of shift in k_x and k_y between the RO^+ and RO^- data. This approach provides a highly accurate shift estimate with sub-pixel resolution while converting the more complicated 2D fitting problem into two 1D fitting problems [33].

RESULTS

Images from an $R = 1$, MB-3, *in vivo* data set are shown in supplementary Figure S2 with three slices highlighted in Fig. 3. The highlighted slices were acquired near regions of known local B_0 inhomogeneity, and residual ghosting is seen in images reconstructed with the online, conventional approach. This ghosting is reduced significantly in the DPoS reconstructions.

Two images from an $R = 2$, MB-3, 2.2 mm isotropic *in vivo* data set are shown in Fig. 4, with the full volume of images shown in supplementary Figure S3. Again, residual ghosting seen in the on-line image reconstructions is again reduced in the DPoS image reconstructions.

In the $R = 3$, MB-2, 1.5 mm isotropic data, we found a significant deterioration in image quality within the conventional image reconstructions in regions known to be near local field inhomogeneity. An example is shown in Fig. 5, where significant ripple artifacts caused by improper ghost correction are seen in the conventionally-reconstructed images. These ripples occur directly above the nasal sinuses—a region with well-known local

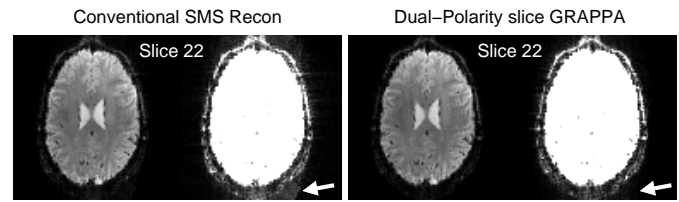


Figure 4. A comparison between current conventional SMS-EPI and DPoS reconstructions from the $R = 2$, MB-3 *in vivo* data. The right-half of each slice shows the lowest 10% of signal to emphasize ghosting. Ghosting levels in the DPoS images are notably lower in regions indicated by arrows. Mosaic images that compare the complete volume are provided in Figure S3, available on-line in the Supplemental files.

B_0 inhomogeneity—as can be seen in the sagittal view, and are removed via DPoS.

Fig. 6 shows plots of the phase difference between RO^+ and RO^- in the 1D phase navigator signals used for conventional NGC, corresponding to two slices (slice 5 and 28) from the images in Fig. 5—one with ripples and one without, with both slices sampled in the same SMS slice-group. The data is shown in x - k_y hybrid-space, from calibration data for two slices in a single slice group, Fig. 6(a) and (b), and from a measured SMS slice group, Fig. 6(c). It is notable that in the lower slice, 5, there is significant non-linearity that confounds the linear phase estimate generated by LPC, shown by the dashed line in Fig. 6(a). By eye, there is a clear linear trend which should be fit by a diagonal line. However, a horizontal linear fit is identified by LPC because, in this example, the amplitudes are highest around $r_x \in [-30, 0]$, which is the region where the linear trend of the phase difference is not as clear. A similar, but smaller, non-linearity is present in the matched SMS slice, 28, which also causes estimation error but to a much lesser degree, Fig. 6(b). This non-linearity is very poorly reflected in the NGC navigator data associated with the measured SMS collapsed slice-group, Fig. 6(c), although some residual estimate bias can still be seen.

DPoS is able to mitigate artifacts caused by non-linear phase errors while simultaneously providing slice-by-slice correction. The benefits of this for fMRI can be seen in 7T images from a separate $R = 3$, MB-2 data set Fig. 7, where ripple artifacts that are present in the on-line reconstructions are removed by DPoS. Consistent with the results in the original demonstration of DPG [13], the presence of ripples in the reconstructed images has a detrimental effect on the signal stability over time and thus the temporal SNR in these regions. This is illustrated in Fig. 7, where the tSNR is markedly lower in the on-line reconstructed image series compared to the DPoS images in regions of B_0 inhomogeneity.

Images reconstructed from the sagittally-zoomed diffusion data acquired at 3T are shown in Fig. 8. In both the $b = 0$ s/mm² and $b = 1000$ s/mm² images, a strong artifact is visible in the conventional reconstructions—e.g. in the axial reformat view. These artifacts are closely associated with strong Nyquist ghosting in the phase-encoding (S-I) direction, visible in the sagittal-plane images. In contrast, the DPoS reconstruction shows a reduction of these ghosts, and a removal of the artifact seen in the axial-reformatted view. Closer inspection of the images recon-

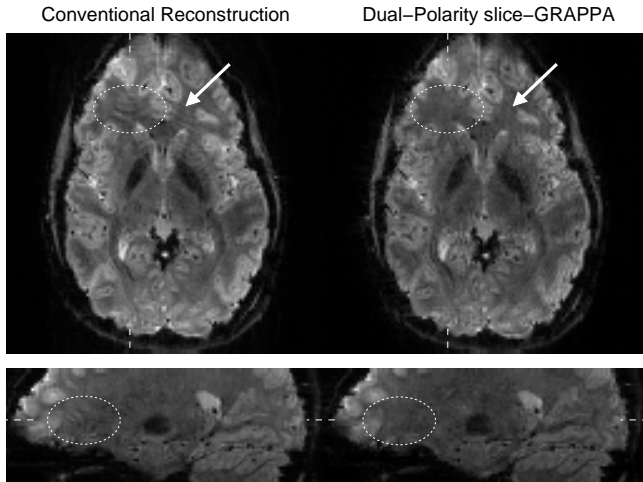


Figure 5. A comparison between conventional slice-GRAPPA reconstruction and DPpG reconstruction from an $R = 3$, MB-2, 1.5 mm isotropic EPI protocol at 7T. Arrows and dashed ovals highlight a region near local B_0 inhomogeneity where ripple artifacts are clearly seen in the conventional image reconstruction. This artifact is removed in the proposed DPpG image reconstruction.

constructed from the calibration data associated with this data set reveals a strong 2D phase error between the RO^+ and RO^- data. This is shown in Fig. 9(a). The reconstructed images and corresponding phase difference between the RO^+ and RO^- images for the three slices in Slice Group 15 are shown in Fig. 9(a). By eye, a phase variation along both x and y directions is clearly visible—the spatial gradient of the phase difference is not strictly parallel to the x direction, as would be expected under the standard linear 1D phase error model. To quantify whether the phase error in x varies across slices, which would necessitate a slice-specific ghost correction, and also whether this additional phase error in the y direction also varies across slices, we estimated the shift in k-space between the RO^+ and RO^- frames of the calibration data. The results are presented in Fig. 9(b), where a clear variation across slices can be seen in both the x and y directions, indicating not only is there slice-specific ghosting but also that the 2D phase error *varies* with slice location. The variation of phase error over the slice direction is relatively smooth and can be approximated by a second-order polynomial function for both the x and y directions, as shown. This indicates that there is a slice-specific 2D phase error, which cannot be addressed by conventional ghost correction methods. However, these slice-dependent 2D phase errors are readily corrected with the DPpG framework.

DISCUSSION

The DPpG approach provides three significant features to the SMS-EPI data reconstruction problem. First, it provides a mechanism to correct for 2D and/or non-linear phase errors between RO^+ and RO^- data without requiring an explicit model of the phase error *a-priori*. Rather, the phase error is modeled implicitly via the GESTE calibration data. We have shown that in addition,

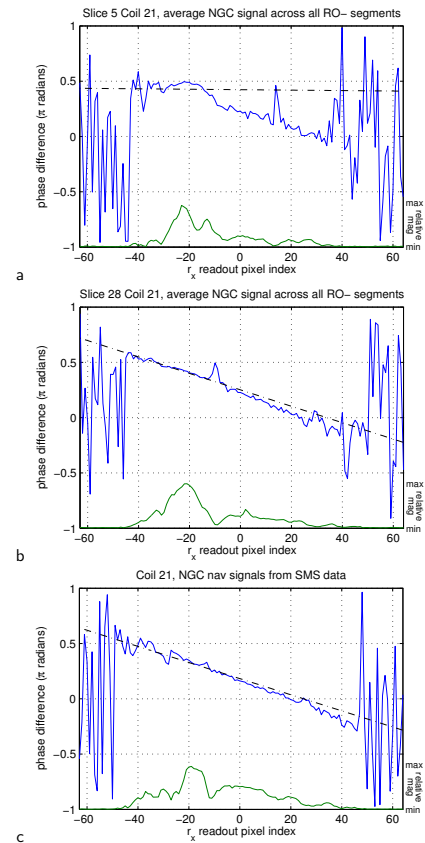


Figure 6. A comparison of phase navigator signals from the $R = 3$, MB-2 *in vivo* data shown in Fig. 5. The phase difference between RO^+ and RO^- navigator signals are shown in blue, with the associated relative magnitude shown in green. The linear fit to the phase difference provided by the LPC method is represented by the dashed line. This method weights the linear fit relative to the navigator signal magnitude. Data for (a) Slice 5, and (b) Slice 28 are taken from the single-band calibration data. Collapsed data from the associated SMS slice-group consisting of these two slices are shown in (c). Notably, significant non-linearity in slice 5—shown in (a)—causes bias in the linear estimate for that slice, resulting in unresolved ghosting.

tion, it can mitigate these errors even when they vary from slice-to-slice. Finally, it can provide both of these benefits through a minor change in the pulse sequence to acquire additional calibration data, and fits seamlessly into current reconstruction implementations by replacing the slice-GRAPPA kernels.

We have demonstrated that SMS applications can benefit from DPpG at both high and ultra-high field. At 3T, DPpG was shown to mitigate 2D phase errors present in an oblique scan plan. At 7T, DPpG was shown to mitigate phase errors caused by local B_0 field inhomogeneities, which increase in severity at ultra-high field and adversely affect EPI reconstructions via both artifacts and sensitivity losses. In both of these cases, the assumptions underling the spatially linear model typically used for Nyquist ghost correction was violated by the imaging scenario, causing a failure in ghost correction. As shown previously with single-slice data [13], the DPpG approach is better able to remove 2D and non-linear phase errors between RO^+ and RO^- data, yielding improved image reconstruction quality.

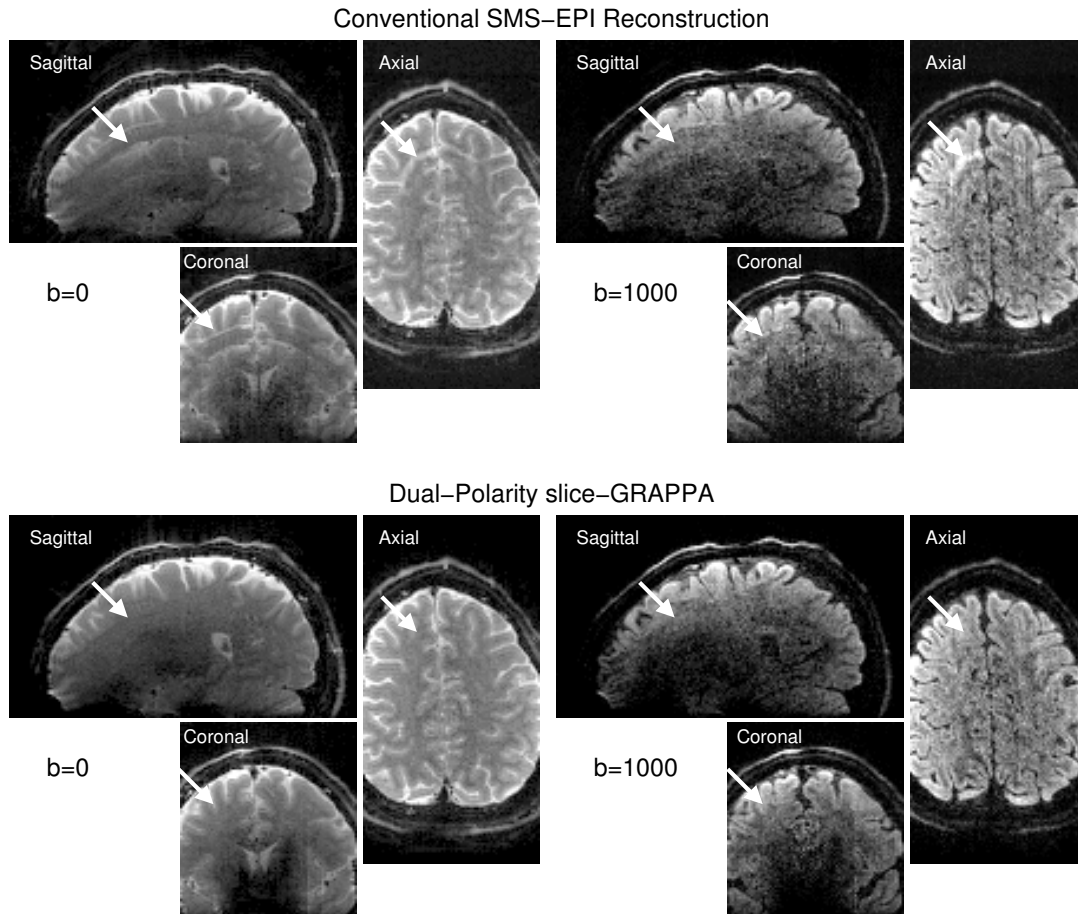


Figure 8. A comparison between conventional slice-GRAPPA image reconstruction and DPsg image reconstruction for sagittally-zoomed SMS-EPI diffusion data, including the $b = 0$ s/mm² reference images and the $b = 1000$ s/mm² diffusion-weighted images. The natively-sagittal data have been reformatted into axial and coronal views to better visualize the residual ghosting artifacts. The arrow indicates edge artifacts associated with unresolved aliasing in the conventional SMS-EPI reconstructions that are removed with the DPsg reconstruction.

The results shown employed a calibration data acquisition order of {segments < polarity < slices}, from inner loop to outer. This ensured that dynamic phase errors caused by subject motion and physiological effects were minimized via FLEET, with the remaining static errors (caused by eddy currents and hardware mis-calibration) removed via GESTE. We note that the optimal ordering of each of the calibration data segments remains an open question that has not yet been fully explored. Similarly, we note that the number of segments suitable for GESTE processing is limited by the number of coils and coil coverage of the multi-channel receiver array. While this may limit the achievable in-plane acceleration that DPsg can accommodate, these limits have not been fully explored. As the in-plane acceleration is increased, the number of data segments needed for calibration will increase and the SNR of the intermediate images within the GESTE process will decrease. Both of these factors may put practical limits on the achievable in-plane acceleration available to DPsg.

The images presented above were generated from the application of a two-stage reconstruction with two sets of GRAPPA kernels: a DPsg kernel set to perform the ghost correction and slice

separation, and an in-plane-GRAPPA kernel set to recover data from in-plane acceleration. The application of slice-GRAPPA and in-plane-GRAPPA kernels is a linear process. Thus, a single set of DPsg kernels could encompass both reconstruction steps and provide similar image reconstruction performance in a single one-stage operation. As GRAPPA employs a convolution operation for reconstruction, such a composite DPG kernel could be formed by an effective convolution of the kernels employed in each stage [34]. However, to achieve an equivalent reconstruction compared to a two-stage reconstruction, the required one-stage kernel would need to be relatively large compared to the size of the two-stage kernels. For example, in the results presented above this would require a kernel comparable to a $3k_y$ -by- $5k_x$ kernel convolved with a $2k_y$ -by- $5k_x$ kernel, yielding a kernel at least $5k_y$ -by- $13k_x$ in size. The extra demand such a large kernel places on processing memory suggests that for practical reasons the two-stage approach is preferred. The two-stage approach also requires a fewer number of kernels, as in-plane acceleration recovery with DPsg in the one-stage approach requires two kernels—one for each possible polarity combination—for each in-plane GRAPPA kernel in the two-

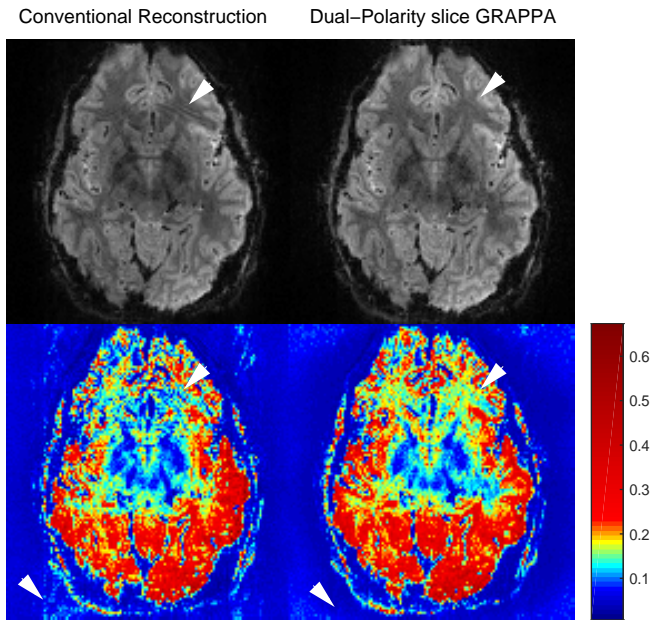


Figure 7. Example comparison between the (left) conventional and (right) DPpG image reconstructions of SMS-EPI data from the $R = 3$, MB-2 *in vivo* data. The top row shows images from Slice 19 with standard windowing. The arrows highlight regions with “ripples” in the conventionally-reconstructed images that are removed by the DPpG reconstruction. The location of the ripple artifact coincides with regions of low tSNR in the conventional reconstructions, as shown in the bottom row. These tSNR maps also exhibit residual ghosting artifacts outside of the brain in the conventional reconstruction that are not seen in the DPpG reconstruction (indicated by arrowheads).

stage approach. This can be visualized in Fig. 2b, where DPpG kernels #2 and #4 could be replaced by a single data-recovery GRAPPA kernel operating in the second stage. In addition, the two-stage approach allows for a more straightforward integration of the DPpG approach for the slice-GRAPPA reconstruction with a traditional in-plane-GRAPPA reconstruction pipeline. A counter consideration is that in a two-stage scheme, errors that potentially occur in the first stage may be amplified in the second stage. Alternatively, the larger kernel size needed for a one-stage kernel may propagate more noise into the reconstruction by virtue of the larger number of coefficients, resulting in less favorable g-factor noise enhancement than could be achieved by the two-stage approach. Currently, the two-stage approach is recommended, due to computation considerations, although this may be revisited more systematically in the future. Regarding computational load, DPpG is comparable to slice-GRAPPA [8], for both the linear system that determines the reconstruction coefficients and their application to slice-accelerated data.

The great challenge of ghost correction in SMS-EPI is known to be the need to identify phase errors for each individual slice, yet only having access to pre-scan data of each independent slice and the collapsed NGC-navigator data in each sampled slice-group. Many solutions have been proposed to address this challenge. Both the two-kernel approach [3] and the 2D-SENSE-GRAPPA method [17] recognized the need to treat RO^+ and

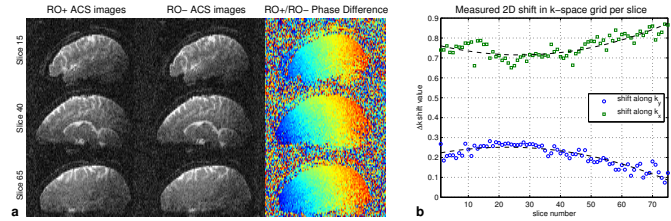


Figure 9. Comparison between RO^+ and RO^- calibration data for the sagittally-zoomed SMS-EPI acquisition shown in Fig. 8. (a) Magnitude images of the calibration data, with the phase difference shown at right. (b) The estimated k-space shift between RO^+ and RO^- data along k_x and k_y . Because shifts in k-space correspond to phase ramps in image-space, these Δk shifts indicate that the phase difference shown in (a) varies relatively smoothly across slices. The dashed black line indicates the best-fitting second-order polynomial fit to the Δk shifts across the slices.

RO^- data separately. In the case of the two-kernel approach [3], the strategy was to perform slice separation on the RO^+ and RO^- data separately in order to preserve the phase errors for later correction. However, this later correction relied on the 1D linear phase error model, which we have shown here to be insufficient for 2D phase errors. The 2D-SENSE-GRAPPA method [17] presented a similar strategy, but employed a model-based modification of the calibration data to characterize the mismatch between RO^+ and RO^- . While this approach was shown to perform well in simulation, the reliance on an explicit model for characterizing phase errors between RO^+ and RO^- data may not generalize well to all cases, potentially including the case of strong nonlinear phase differences seen around B0 inhomogeneity regions in our 7T data. Future work will test whether the 2D-SENSE-GRAPPA slice separation model can be constructed from DPpG calibration data, to enable a DPpG-like SENSE-based SMS reconstruction.

CONCLUSIONS

We have demonstrated that the DPG approach to EPI reconstruction, originally developed for reconstructing conventional single-slice EPI data with in-plane acceleration, can be extended to SMS-EPI reconstruction. This method provides ghost correction improvements to SMS-EPI data, in both in-plane-accelerated and un-accelerated cases, comparable to the results seen previously when DPG was applied to conventional single-slice EPI. DPpG can perform slice separation and slice-specific ghost correction simultaneously in one step. In addition, data recovery of in-plane accelerated data can also be performed if desired. The application of this method to functional, diffusion, and perfusion MRI is forthcoming.

ACKNOWLEDGMENTS

Support for this work was provided in part by the Functional Neuroimaging Laboratory at the Brigham and Women’s Hospital, by the NIH National Institute for Biomedical Imaging and Bioengineering (grants P41-EB015896 [PI: Rosen], R01-EB019437 [PI: Polimeni] and R01-EB020613 [PI: Setsompop]),

by the BRAIN Initiative (NIH National Institute of Mental Health grant R01-MH111419 [PI: Polimeni]), and by the MGH/HST Athinoula A. Martinos Center for Biomedical Imaging, and was made possible by the resources provided by NIH Shared Instrumentation Grants S10-RR023401, S10-RR019307, S10-RR019371, and S10-RR020948. We also thank Dr. Thomas Witzel for his help in acquiring the sagittally-zoomed diffusion data.

REFERENCES

- Nunes RG, Hajnal JV, Golay X, Larkman DJ. Simultaneous slice excitation and reconstruction for single shot EPI. in *Proc ISMRM 14th Annual Meeting*. 2006; 293.
- Moeller S, Yacoub E, Olman CA, Auerbach E, Strupp J, Harel N, Ugurbil K. Multiband multislice GE-EPI at 7 tesla, with 16-fold acceleration using partial parallel imaging with application to high spatial and temporal whole-brain fMRI. *Magn Reson Med* 2010;63(5):1144–1153.
- Setsompop K, Cohen-Adad J, Gagoski BA, Raij T, Yendiki A, Keil B, Wedeen VJ, Wald LL. Improving diffusion MRI using simultaneous multi-slice echo planar imaging. *NeuroImage* 2012;63(1):569 – 580.
- Feinberg DA, Setsompop K. Ultra-fast MRI of the human brain with simultaneous multi-slice imaging. *Journal of Magnetic Resonance* 2013; 229:90–100. *Frontiers of In-Vivo and Materials {MRI} Research*.
- Barth M, Breuer F, Koopmans PJ, Norris DG, Poser BA. Simultaneous multislice (SMS) imaging techniques. *Magn Reson Med* 2016;75(1):63–81.
- Larkman DJ, Hajnal JV, Herlihy AH, Coutts GA, Young IR, Ehnholm G. Use of multicoil arrays for separation of signal from multiple slices simultaneously excited. *J Magn Reson Imaging* 2001;13(2):313–317.
- Feinberg DA, Moeller S, Smith SM, Auerbach E, Ramanna S, Gunther M, Glasser MF, Miller KL, Ugurbil K, Yacoub E. Multiplexed echo planar imaging for sub-second whole brain fMRI and fast diffusion imaging. *PLoS ONE* 2010;5(21):e15710–20.
- Setsompop K, Gagoski BA, Polimeni JR, Witzel T, Wedeen VJ, Wald LL. Blipped-controlled aliasing in parallel imaging for simultaneous multislice echo planar imaging with reduced g-factor penalty. *Magn Reson Med* 2012;67(5):1210–1224.
- Zahneisen B, Ernst T, Poser BA. SENSE and simultaneous multislice imaging. *Magnetic Resonance in Medicine* 2015;74(5):1356–62.
- Larkman DJ, Nunes RG. Parallel magnetic resonance imaging. *Phys in Medicine and Biology* 2007;52(7):R15–R55.
- Breuer FA, Blaimer M, Heidemann RM, Mueller MF, Griswold MA, Jakob PM. Controlled aliasing in parallel imaging results in higher acceleration (CAIPIRINHA) for multi-slice imaging. *Magnetic Resonance in Medicine* 2005;53(3):684–691.
- Moeller S, Auerbach E, Vu AT, Lenglet C, Sotiropoulos SN, Ugurbil K, Yacoub E. EPI 2D ghost correction and integration with multiband : application to diffusion imaging at 7t. in *Proc ISMRM 23rd Annual Meeting*. Toronto, ON, CA, 2015; 248.
- Hoge WS, Polimeni JR. Dual-polarity GRAPPA for simultaneous reconstruction and ghost correction of EPI data. *Magn Reson Med* 2016; 76(1):32–44.
- Xu D, Maier JK, King KF, Collick BD, Wu G, Peters RD, Hinks RS. Prospective and retrospective high order eddy current mitigation for diffusion weighted echo planar imaging. *Magn Reson Med* 2013;70(5):1293–1305.
- Zhu K, Dougherty RF, Takahashi AM, Pauly JM, Kerr AB. Nyquist ghosting correction for simultaneous multislice echo planar imaging. in *Proc of the 22nd Annual Meeting of ISMRM*. Milan, Italy, 2014; 647.
- Hennel F, Buehrer M, von Deuster C, Seuen A, Pruessmann KP. SENSE reconstruction for multiband EPI including slice-dependent N/2 ghost correction. *Magn Reson Med* 2016;76(3):873–879.
- Koopmans PJ. Two-dimensional-NGC-SENSE-GRAPPA for fast, ghosting-robust reconstruction of in-plane and slice-accelerated blipped-CAIPI echo planar imaging. *Magnetic Resonance in Medicine* 2017; 77(3):998–1009.
- Setsompop K, Kimmlingen R, Eberlein E, Witzel T, Cohen-Adad J, McNab JA, Keil B, Tisdall MD, Hoecht P, Dietz P, Cauley SF, Tountcheva V, Matschl V, Lenz VH, Heberlein K, Potthast A, Thein H, Van Horn J, Toga A, Schmitt F, Lehne D, Rosen BR, Wedeen V, Wald LL. Pushing the limits of in vivo diffusion MRI for the Human Connectome Project. *NeuroImage* 2013;80(Supplement C):220 – 233. Mapping the Connectome.
- Griswold MA, Jakob PM, Heidemann RM, Nittka M, Jellus V, Wang J, Kiefer B, Haase A. Generalized autocalibrating partially parallel acquisitions (GRAPPA). *Magn Reson Med* 2002;47(6):1202–1210.
- Cauley SF, Polimeni JR, Bhat H, Wald LL, Setsompop K. Interslice leakage artifact reduction technique for simultaneous multislice acquisitions. *Magnetic Resonance in Medicine* 2014;72(1):93–102.
- Xu J, Moeller S, Auerbach EJ, Strupp J, Smith SM, Feinberg DA, Yacoub E, Ugurbil K. Evaluation of slice accelerations using multiband echo planar imaging at 3 T. *NeuroImage* 2013;83:991 – 1001.
- Todd N, Moeller S, Auerbach EJ, Yacoub E, Flandin G, Weiskopf N. Evaluation of 2D multiband EPI imaging for high-resolution, whole-brain, task-based fmri studies at 3T: Sensitivity and slice leakage artifacts. *NeuroImage* 2016;124, Part A:32 – 42.
- Hoge WS, Tan H, Kraft RA. Robust EPI Nyquist ghost elimination via spatial and temporal encoding. *Magn Reson Med* 2010;64(6):1781–1791.
- Polimeni JR, Bhat H, Witzel T, Benner T, Feiweier T, Inati SJ, Renvall V, Heberlein K, Wald LL. Reducing sensitivity losses due to respiration and motion in accelerated Echo Planar Imaging by reordering the autocalibration data acquisition. *Magn Reson Med* 2016;75(2):665–679.
- Polimeni JR, Setsompop K, Hoge WS. Characterization of autocalibration methods for accelerated EPI reconstructions using GRAPPA. *Proc Intl Soc Mag Reson Med* 2014;4397.
- Keil B, Triantafyllou C, Hamm M, Wald LL. Design optimization of a 32-channel head coil at 7T. in *Proc of 18th Annual Meeting of ISMRM*. Stockholm, Sweden, 2010; 1493.
- McNab JA, Edlow BL, Witzel T, Huang SY, Himanshu B, Heberlein K, Feiweier T, Liu K, Keil B, Cohen-Adad J, Tisdall MD, Folkner RD, Kinney HC, Wald LL. The Human Connectome Project and beyond: Initial applications of 300 mT/m gradients. *NeuroImage* 2013;80:234 – 245. Mapping the Connectome.
- Keil B, Blau JN, Biber S, Hoecht P, Tountcheva V, Setsompop K, Triantafyllou C, Wald LL. A 64-channel 3T array coil for accelerated brain MRI. *Magnetic Resonance in Medicine* 2013;70(1):248–258.
- Heidemann RM, Anwender A, Feiweier T, Knösche TR, Turner R. k-space and q-space: Combining ultra-high spatial and angular resolution in diffusion imaging using ZOOMPPA at 7 T. *NeuroImage* 2012;60(2):967 – 978.
- Setsompop K, Fan Q, Stockmann J, Bilgic B, Huang S, Cauley SF, Nummenmaa A, Wang F, Rathi Y, Witzel T, Wald LL. High-resolution in vivo diffusion imaging of the human brain with generalized slice dithered enhanced resolution: Simultaneous multislice (gSlider-SMS). *Magnetic Resonance in Medicine* 2017;n/a–n/a.
- Feiweier T. Magnetic resonance method and apparatus to determine phase correction parameters, 2013. US Patent 8,497,681.
- Buehrer M, Boesiger P, Kozerke S. Virtual body coil calibration for phased-array imaging. in *Proceedings 17th ISMRM Scientific Meeting*. Honolulu, HI, 2009; 759.
- Hoge WS. Subspace identification extension to the phase correlation method. *IEEE Trans on Medical Imaging* 2003;22(2):277–280.
- Griswold MA, Blaimer M, Breuer F, Heidemann RM, Mueller M, Jakob PM. Parallel magnetic resonance imaging using the GRAPPA operator formalism. *Magn Reson Med* 2005;54(6):1553–1556.

List of Supporting Figures

- Signal flow diagram illustrating DPsg kernel calibration for an acquisition with in-plane acceleration factor R and slice acceleration factor (or MultiBand factor) MB . (A) Preparation of ghost-free training data from the temporally-encoded segmented EPI calibration data. (B) Synthetic SMS data are then generated and used as source data for the DPsg calibration, while target data consists of ghost-free data. Only the signal flow for slice-group n , slice m is shown.
- A comparison between current conventional SMS-EPI image reconstruction and DPsg image reconstruction from the $R = 1$, $MB=3$ *in vivo* data. The mosaic images are organized by slice group along the columns, with three example slices highlighted at the bottom. The right-half of each slice shows the lowest 10% of signal to emphasize ghosting. Ghosting levels in the DPsg images are notably lower in regions indicated by arrows.
- A comparison between current conventional SMS-EPI and DPsg reconstructions from the $R = 2$, $MB=3$ *in vivo* data. The right-half of each slice shows the lowest 10% of signal to emphasize ghosting. Ghosting levels in the DPsg images are notably lower in regions indicated by arrows.

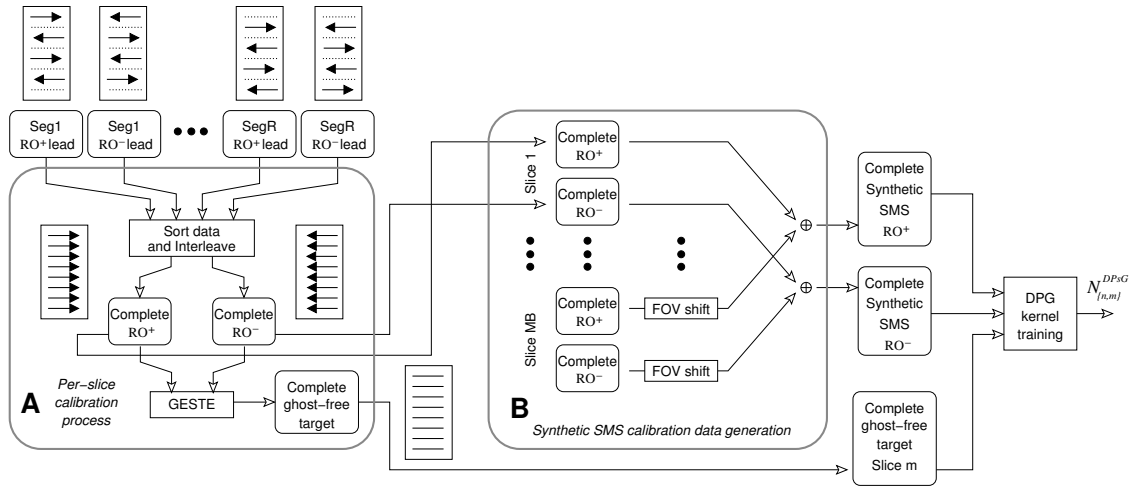


Figure S1. Signal flow diagram illustrating DP&gD kernel calibration for an acquisition with in-plane acceleration factor R and slice acceleration factor (or MultiBand factor) MB . (A) Preparation of ghost-free training data from the temporally-encoded segmented EPI calibration data. (B) Synthetic SMS data are then generated and used as source data for the DP&gD calibration, while target data consists of ghost-free data. Only the signal flow for slice-group n , slice m is shown.

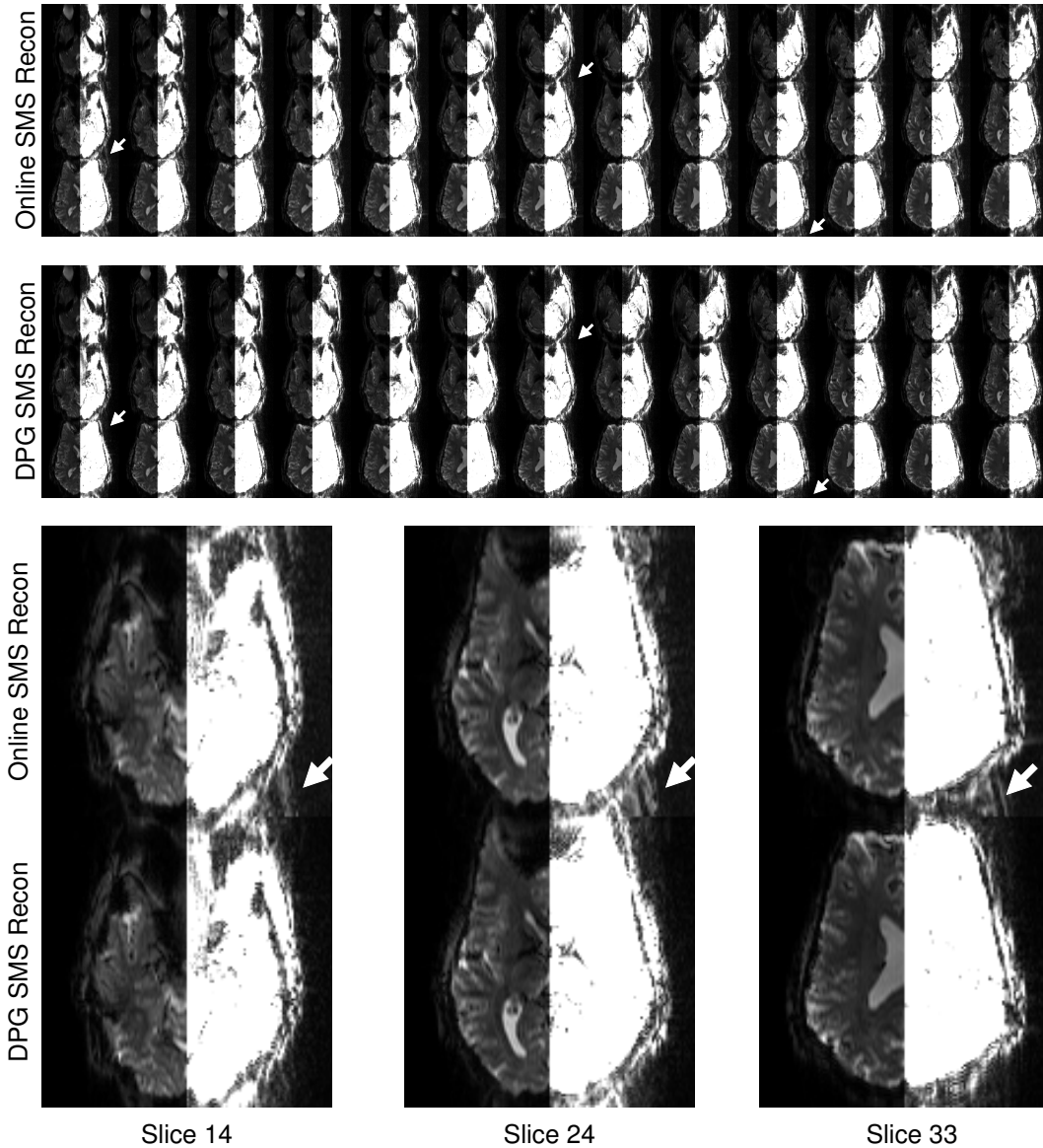


Figure S2. A comparison between current conventional SMS-EPI image reconstruction and DPoS image reconstruction from the $R = 1$, MB-3 *in vivo* data. The mosaic images are organized by slice group along the columns, with three example slices highlighted at the bottom. The right-half of each slice shows the lowest 10% of signal to emphasize ghosting. Ghosting levels in the DPoS images are notably lower in regions indicated by arrows.

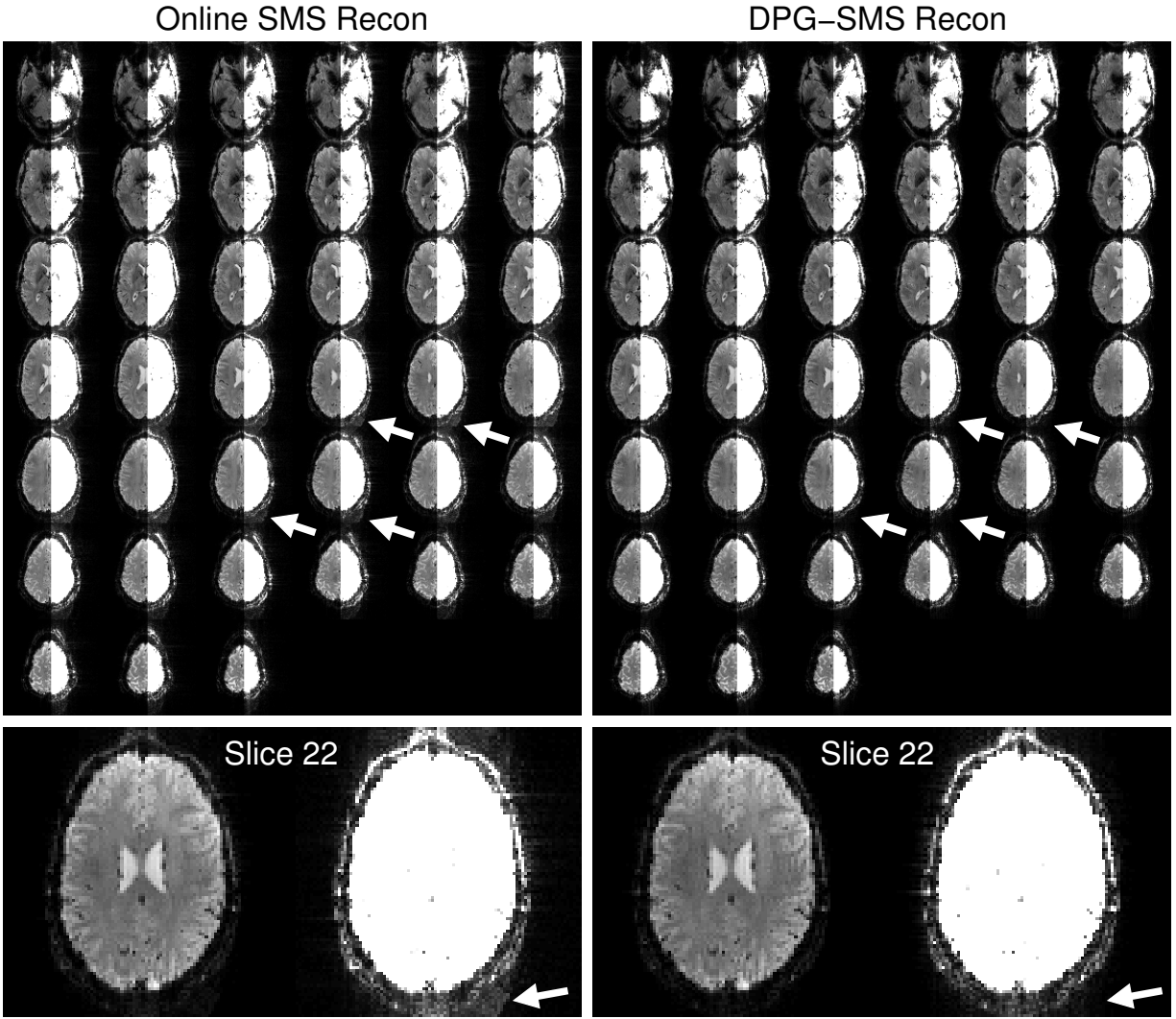


Figure S3. A comparison between current conventional SMS-EPI and DP_sG reconstructions from the $R = 2$, MB-3 *in vivo* data. The right-half of each slice shows the lowest 10% of signal to emphasize ghosting. Ghosting levels in the DP_sG images are notably lower in regions indicated by arrows.